This is a preprint, the final version is subject to change, of the American Mineralogist (MSA)
Cite as Authors (Year) Title. American Mineralogist, in press.
(DOI will not work until issue is live.) DOI: http://dx.doi.org/10.2138/am.2013.4170

Revision 1

Natural occurrence of keatite precipitates in UHP clinopyroxene from the Kokchetav Massif: A TEM investigation

Tina R. Hill, Hiromi Konishi, and Huifang Xu *

Department of Geoscience, University of Wisconsin-Madison, Madison, Wisconsin 53706, U.S.A.

*Corresponding author

Always consult and cite the final, published document. See http://www.minsocam.org or GeoscienceWorld

ABSTRACT

We report the first natural occurrence of keatite, also known as silica K, discovered as a precipitate in the core of ultrahigh-pressure (UHP) clinopyroxene (CPX) within garnet pyroxenite from the Kokchetav Massif, Kazakhstan. High-resolution transmission electron microscopy and electron diffraction demonstrate that sub-micron and nano-scale keatite precipitates have a definite crystallographic relationship with the host pyroxene (diopside = ~Di_{89}) CPX (100) ‖ keatite (100) and CPX (010) ‖ keatite (001). Clinopyroxene provides a template for keatite nucleation due to the close structural relationship and excellent lattice match between the diopside and keatite. We propose that keatite micro-precipitates are formed in localized low pressure micro-environments produced as a result of exsolution of extra silica and vacancies held within UHP host diopside and stabilized by the pyroxene lattice. Low density metastable keatite and its relationship to the host pyroxene likely reflects the important influence of pyroxene/precipitate interfacial energy on the micro- and nano-scales in controlling the nature of exsolved phases in exhumed UHP minerals.

Keywords: HRTEM, ultrahigh-pressure (UHP), diopside, keatite, silica exsolution, epitaxial growth

1. INTRODUCTION

Keatite, a metastable polymorph of silica, has been synthesized experimentally using hydrothermal methods at low pressure, but was not confirmed in nature. Oriented silica precipitates are a relatively common feature in clinopyroxenes from high- and ultrahigh-pressure rocks and have been noted in numerous collisional orogenic rocks, and are generally identified as quartz (Smith 1984; Gayk, et al. 1995; Liou, et al. 1998; Katayama, et al. 2000; Dobrzhinetskaya, et al. 2002; Zhang, et al. 2005; Proyer, et al. 2009). High pressure and ultrahigh-pressure clinopyroxenes are of great interest for studying physical and chemical characteristics of rocks subducted to or formed at upper mantle depths and returned to Earth's surface. Oriented silica precipitates inside the clinopyroxenes have been used as indicators of these UHP conditions, sometimes in the absence of direct mineralogical evidence (diamond or coesite). Direct characterization of the exsolved minerals is necessary, and this study is the first to characterize these silica precipitates utilizing high resolution transmission electron microscopy. The advantage of HRTEM is its ability to unite crystallography, crystal size, *and* chemistry, and has permitted identification of the nano-scale metastable keatite phase.

The keatite discovered in this study was observed in the core of an UHP clinopyroxene within a micro-diamond-bearing garnet pyroxenite. This garnet pyroxenite exists as thin lenticular bands or lens-like bodies within plagioclase gneisses of the Zerenda rock series (Kumdy Kol region) from the Kokchetav Massif, Kazakhstan. Peak metamorphic *P*-*T* estimates of these rocks yield minimum pressures of 40 kbar and temperatures exceeding 900°C (Shatsky, et al. 1995). The rocks have undergone pervasive retrograde metamorphism to amphibolite facies, preserving only rare UHP mineral assemblages within refractory minerals such as garnet and zircon (Sobolev, et al. 1994).

This rock is dominated by clinopyroxene and garnet, with accessory minerals of rutile, Fe-oxides, apatite, and zircon. The texture of the rock is medium-grained, massive, and generally equigranular. The rock is relatively fresh, but has minor fractures filled with sheet silicates, quartz, feldspar, and carbonates. Transmitted light photomicrographs of clinopyroxene grains show siliceous precipitates concentrated in cores of the crystals (Fig. 1). Optically, no minerals other than silica were observed. Figure 1a shows a clinopyroxene oriented with the *c*-axis approximately normal to the plane of the image. This orientation causes the precipitates to appear as dark euhedral dots. In two different clinopyroxene grains viewed at a high angle to the *c*-axis, the precipitates appear as elongated rods (Fig. 1b). This image highlights the concentration of precipitates in the cores of clinopyroxene; they are rarely seen in the rims. Later stage retrograde reactions are sometimes seen at the boundaries of grains in the garnet pyroxenite.

Keatite, or silica K, is an atypical crystal with a negative overall thermal expansion coefficient (Keat 1954). Initial synthesis by Keat (1954) was at experimental conditions of 0.33-1.1 kbar and 380-585°C; more recent experiments agree that crystallization is favored at moderate temperatures (200°-400°C) and pressures (2-3 kbar) (Bettermann and Liebau 1975). Formation environment composition is extremely important for keatite synthesis, and it has been synthesized utilizing a variety of siliceous starter materials. Experiments resulting in keatite include hydrothermal synthesis from dilute aqueous alkaline solutions (Keat 1954), amorphous silica reaction with H_2O mimicking the diagenesis of amorphous silica to quartz (Carr and Fyfe, 1958), and silica glass plus cristobalite in water solution (White and Corwin 1961; Bettermann and Liebau 1975; Martin 1995). Weakly alkaline solutions seem to be a requirement for its formation; overly dilute solutions lead to the precipitation of cristobalite and high concentrations induce the crystallization of quartz (Keat 1954). Some studies suggest that pressure may be more important than temperature in determining keatite formation (Carr and Fyfe 1958; White and Corwin 1961). This paper details characterization of the structural relationship at the diopside (CPX)/keatite micro-crystal interface, and seeks to explain why natural keatite has formed in ultrahigh-pressure (UHP) clinopyroxene to the exclusion of other SiO_2 polymorphs. One instance of possible natural keatite was reported in airborne volcanic particles (Rietmeijer 1988); however, analysis of both composition and powder electron diffraction patterns has not confirmed this observation (Heaney 1994).

2. EXPERIMENTAL METHODS

Major element compositions of bulk clinopyroxene crystals were determined using a Cameca SX51 electron microprobe at the University of Wisconsin-Madison. Analytical conditions were 15 kV accelerating voltage, Faraday cup current of 20 nA, and 20 s counting times per element. Beam spot size was 1 μm. Microprobe analytical standards were: hematite for Fe, augite for Ca, olivine for Mg, rutile for Ti, chromite for Cr, Mn-olivine for Mn, and hornblende for Si, Na, Al, and K. Petrographic thin sections polished to 30 μm thick were used to find clinopyroxene grains oriented looking parallel to the *c*-axis with precipitates in the cores. The clinopyroxene grains were cut out and thinned to ~20 μm by hand with silicon carbide grinding disks. Grains were then mounted on molybdenum TEM grids. These foils were thinned to electron transparency via Ar^+ ion milling in a Fischione 1010 ion mill. High-resolution TEM (HRTEM) images and selected area electron diffraction patterns (SAED) were obtained utilizing the FEI Titan aberration-corrected S/TEM at 200 kV accelerating voltage. In addition to clinopyroxene chemical compositions from the electron microprobe, compositions of silica precipitates were analyzed by means of X-ray energy-dispersive spectroscopy (EDS) from the specimen with small spot sizes using an EDAX EDS system. This EDS system is attached to the FEI Titan S/TEM operated at 200 kV accelerating voltage. Clinopyroxene X-ray diffraction (XRD) patterns were collected with a Rigaku Rapid II X-ray diffraction system with a 2-D image plate (Mo Kα radiation), with an accelerating voltage of 50kV, a current of 50 mA, and a 0.1mm diameter collimator. Diffraction data were collected on an image-plate detector. Two-dimensional images were then integrated to produce conventional 2-theta -intensity patterns using Rigaku's 2DP software. Clinopyroxene lattice parameters were refined with least squares analysis using MDI, Inc. Jade 9.0 software.

3. RESULTS

3.1 Electron Microprobe

Table 1 presents recalculation EMPA data from a representative clinopyroxene grain in the Kokchetav Massif garnet pyroxenite. Standard deviation and standard error of these data are reported (SDEV= Standard deviation, SERR=Standard error, and n=14). Oxygen was calculated, not measured, and all calculations are normalized to six O atoms. All clinopyroxenes analyzed via electron microprobe (EMPA) exhibit silica precipitates in their cores. Nearly all spots analyzed show sufficient Al to fill the ^{IV}Al, the rest fills ^{VI}Al. The clinopyroxene is highly calcic (~Di_{90}), with little Na and very little to no K. In this paper, we broadly constrain vacancy content in clinopyroxene grains by assuming vacancy plus insufficient cations sums to four; non-stoichiometric pyroxenes possess <4 total cations. We report a possible minimum vacancy component ([]) in Table 1 in which all Fe is calculated as Fe^{2+}.

3.2 TEM Results

The TEM image of a natural crystal of keatite (light phase) in clinopyroxene (dark phase) (Fig. 2a) shows evidence of a euhedral ‘negative’ pyroxene crystal shape, not a euhedral silica crystal shape. Crystallographic planes exhibited are the dominant pyroxene crystallographic forms of {010}, {100}, and {110} typically seen in euhedral pyroxenes at all scales. Nearly all precipitates found exhibit this shape. Orientation relationships of all three phases, clinopyroxene (no arrows, zone axis [001]) with amphibole (right-pointing black arrows, zone axis [001]) and keatite (white left-pointing arrows, zone axis [010]), are demonstrated in the SAED pattern (Fig. 2b). Clinopyroxene lattice parameters calculated after collecting X-ray diffraction data from a single crystal of clinopyroxene and refined via least squares method are: $a = 9.754$ Å, $b = 8.921$ Å, $c = 5.244$ Å, $\alpha = \gamma = 90°$, $\beta = 105.9°$. When calibrated to these parameters, analysis of the SAED pattern shows pyroxene is diopside with space group *C2/c*, and produces two orthogonal lattice parameters of the silica precipitate: $a = 7.47$Å, $c = 8.58$Å. These parameters are only consistent with published crystallographic data from SiO_2 polymorph keatite ($a = b = 7.456$ Å, $c = 8.604$ Å (Keat, 1954)). Schematic indexing of keatite (Fig. 2c), and keatite plus clinopyroxene

(Fig. 4d) confirms that the SAED pattern (Fig. 4b) matches keatite zone axis [010]. Keatite diffraction spots (100) and (001) which appear in the SAED pattern are typically at extinction but appear due to multiple diffraction effects in here. They are identified as X's in Fig. 2. X-ray EDS spectrum from the silica precipitate (inset Fig. 2a) also confirms a silica polymorph. Carbon peak is from coated carbon. Amphibole formed at the interface of clinopyroxene and keatite is in epitaxy with both minerals. HRTEM image of the clinopyroxene/amphibole interface (Fig. 3) demonstrates the close structural relationship between host clinopyroxene and amphibole. Fast Fourier Transform (FFT) patterns of both clinopyroxene and amphibole (Fig. 3b) match to diffraction spots from host pyroxene and amphibole precipitate in the SAED pattern (Fig. 2b). Graphic representation of the crystallographic relationship between clinopyroxene and keatite derived from the SAED pattern illustrates epitaxial growth of keatite on clinopyroxene (Fig. 4). Fig. 4a and 4c are the same orientations: $[001]_{\mathrm{CPX}} \parallel [100]_{\mathrm{keatite}}$. The initial layer (Fig. 4a) of keatite tetrahedra (green) bonding to clinopyroxene tetrahedra (blue) closely matches clinopyroxene lattice dimensions with systematic gaps of keatite tetrahedra in the structure. Some charge will be unsatisfied in these models where systematic silica tetrahedra absences reside. Subsequent layers of silica tetrahedra have been added to the layered structure in Figure 4c; the systematic absence of silica tetrahedra on the initial bonding layer is very clear here. The systematic absences can also be seen clearly in an *a*-*b* clinopyroxene section (Fig. 4b). The tetrahedra bond with little change in orientation or rotation. Red arrows in all orientations of Fig. 4 models denote the location of the first layer of bonding for reference. A comparison of the clinopyroxene/keatite unit cells (Fig. 4d, same orientation as in a and c) along clinopyroxene *b*-axis and keatite *c*-axis demonstrates that the clinopyroxene lattice is a mere 3.5% larger than keatite over just one unit cell, and exhibits even less difference in the keatite *b*-

axis/clinopyroxene *c*-axis direction. A basic calculation of the total lattice misfit based upon d-spacings and unit cell area of both clinopyroxene [001] and keatite [010] yields a total crystal misfit of only 5.1 %.

Phyllosilicates were observed in close proximity to some silica precipitates (Fig. 5a) in this investigation. In these precipitates, the shape appears somewhat modified from the euhedral 'negative' pyroxene shape seen in Fig. 2a, with the sheet silicates either fully covering a silica precipitate or simply taking on the euhedral pyroxene shape itself. The composition of this area is not straightforward. Spot 1 on Fig. 5a is compositionally Si and O, but, surprisingly, the HRTEM lattice image at spot 1 indicated by an arrow (inset in Fig.5b) clearly shows a layered structure. Not far away, at spot 2, EDS analysis shows a typical mica composition, but a relatively high amount of silica (Fig. 5c). In these precipitates where micas have overgrown silica, {110} faces of the negative pyroxene are either not well-developed or degraded; a white arrow in Fig. 5a points to a degraded (110) plane, and another is labeled. When compared to precipitate shape in Fig. 2, the degradation of {110} faces can be easily observed. Numbered spots 3 and 4 in Fig. 5, seen up close in HRTEM images of the amphibole/clinopyroxene interface (Fig. 6e) and the mica/clinopyroxene interface (Fig. 6f) detail the similarities and differences between the now-typical silica precipitate and the degraded precipitate. HRTEM image of mica (Fig. 6f) shows the layering of the mica, but no silica, and displays a degraded (110) pyroxene face. Clinopyroxene, amphibole, and mica possess parallel (010) planes, and $(100)_{CPX} \parallel (001)_{mica}$. In addition to the EDS pattern (spot 2, Fig. 5a), the SAED pattern (Fig. 6c) obtained from a smaller area of the Fig. 5 precipitate confirms a siliceous mica. The nano-scale amphibole (Spot 3, Fig.5a and Fig 6e) exhibits the same epitaxial orientation to clinopyroxene as observed in Fig. 3: $[001]_{CPX} \parallel [001]_{amph}$, $(010)_{CPX} \parallel (010)_{amph}$. SAED pattern simulations of clinopyroxene/amphibole/mica (Fig. 6b) and mica (Fig. 6d) electron diffraction patterns match the SAED patterns and the epitaxial relationship of the three phases.

4. DISCUSSION

Fig. 2 demonstrates clearly that this silica polymorph is keatite, not the expected higher density polymorphs, coesite or quartz, previous researchers have reported in UHP clinopyroxenes. Oriented silica in clinopyroxene from high- and ultrahigh-pressure pyroxenes, such as that investigated in this study, is widely interpreted as the result of exsolution of excess silica from host clinopyroxene during decompression via the reaction:

$$2Ca_{0.5}\square_{0.5}AlSi_2O_6 = CaAl_2SiO_6 + 3SiO_2$$

($Ca_{0.5}\square_{0.5}AlSi_2O_6$= CaEskola (CaEs) vacancy solid solution in pyroxene, and $\square$ = vacancy)

(Smyth 1980; Liou, et al. 1998; Dobrzhinetskaya, et al. 2002; Klemd 2003; Zhang, et al. 2005; Zhao, et al. 2011), but this does not explain why keatite has formed to the exclusion of other silica polymorphs. We interpret keatite as a primary exsolution feature on the retrograde path during slab exhumation. Keatite likely forms due to nano-scale size effects, interface-controlled exsolution controlled by host clinopyroxene, and an unusual exsolution environment created by density changes and exsolved vacancies from the diopside structure.

Experimentally, it is energetically more favorable to exsolve keatite prior to quartz, and the transformation of keatite → quartz appears to occur more rapidly than transformations of quartz → keatite (Carr and Fyfe 1958). This experimental keatite → quartz relation is well-documented (Carr and Fyfe 1958; White and Corwin 1961; Martin 1995). Accurate determination of silica exsolution depth is impossible with the data at hand; however keatite formation is restricted to low pressure, higher temperature environments (Keat 1954; Bettermann and Liebau 1975). We may rule out exsolution at or near the surface of the Earth. This is kinetically and thermodynamically unfeasible, and keatite would likely transform quickly to quartz.

In addition, nano-scale size effects likely affect the *P*-*T* regime at which this crystal of keatite occurs. Research shows that mineral nano-particles commonly behave differently as a function of their size within the nano-scale range. Mineral nano-particles also behave differently than larger micro- and macroscopic crystals of the same structure and composition. At the nano-scale, three factors compete to stabilize a given polymorph: enthalpy of polymorphic transition, surface enthalpy, and enthalpy of hydration (Hochella, et al. 2008). Navrotsky (2004) reported that competition between surface enthalpy and the energetics of phase transformation leads to the general conclusion that polymorphs that are metastable as micron-sized or larger crystals can often be thermodynamically stabilized at the nano-scale. This phenomenon has been observed in TiO_2 polymorphs and iron oxides, among others (Navrotsky 2004; Chen and Fu 2006; Barnard and Xu 2008). Thus, we infer metastable nano-scale keatite may be stabilized at some depth in part due to its small size.

In combination with nano-scale size effects, mechanisms of exsolution are closely related to the types of interfaces that develop between two phases. The geometry of the substrate in epitaxial mineral growth is known to cause growth of phases not stable at existing *P*-*T*-X conditions. Keatite exsolution shape is certainly dominated by the clinopyroxene, and a high degree of lattice match between the two likely serves to stabilize the nano-scale keatite crystal. Electron diffraction (Fig. 2b) illustrates epitaxy in two directions, where CPX (100) ‖keatite (100), and CPX (010) ‖keatite (001). Epitaxial nucleation of phases on dominant crystal faces (such as pyroxene {010} and {100} seen in this study) creates structural coherency and excellent lattice matching across the mineral interface. Our schematic lattice model of these interfaces demonstrates the maximum percentage of lattice mismatch along unit cells is just 3.5 % (Fig.4d). In addition, the flexibility of the silica tetrahedra in chain silicate structures can provide stable geometric configurations with a very extensive range of cations and over a wide range of temperature and pressure conditions (Burnham, et al. 1967; Cameron and Papike 1981). Similarly, silica tetrahedra are well known to bend and rotate (Hochli and Scott 1971; Megaw 1973). As a result, silica tetrahedra at the interface can twist and bend to accommodate small lattice differences. Even a systematic absence of the green keatite silica tetrahedra, which can be seen on the first layer of blue pyroxene tetrahedra (Fig. 4a) can provide accommodation of mismatch. Therefore, lattice strain may be reduced, minimizing energy required for nucleation and growth of the metastable silica phase.

Presence of epitaxially-oriented amphibole at the interface of clinopyroxene and silica may also hold clues to formation (Fig. 2 orientations: pyroxene (010) ‖amphibole (010)‖keatite (001)). Two possibilities for exsolution of silica + amphibole in clinopyroxene have been presented. 1) Shau, et al. (2005) proposed a two-stage growth mechanism of silica/amphibole — decompression-related silica exsolution from pyroxene containing a CaEs component, followed by simultaneous amphibole + silica growth as a result of clinopyroxene breakdown along silica/clinopyroxene interface. 2) Page, et al. (2005) proposed formation of amphibole + silica may form in a clinopyroxene without a CaEs component by retrogressive breakdown of clinopyroxene. In a study of three eclogites from the Saualpe and Pohorje Mountains, Konzett, et al. (2008) concluded that, with combined textural and chemical information, formation of intergrown calcic amphibole/oriented quartz inclusions in cores of clinopyroxene was unrelated to a breakdown of the CaEs component in one rock; however, the involvement of a Ca-Eskola component could not be ruled out in one of the eclogites. Due to lack of volume change at exsolution sites and freshness of the interfaces between amphibole, clinopyroxene, and silica, number one may be most likely possibility for keatite.

Another example of multiphase inclusions in Kokchetav Massif clinopyroxenes and garnets from diamondiferous garnet/clinopyroxene rocks are assemblages of K-bearing kokchetavite, phengite, cristobalite, and an amorphous phase. Formation of these assemblages is interpreted from melts intruding though partings and cleavages of pyroxene, rather than exsolution (Hwang, et al. 2004). Although the assemblages appear similar at first, this is unlikely the mechanism of formation for the silica in this study for several reasons. 1) lack of sufficient K in the primary unaltered keatite and other silica precipitates to indicate sufficient fluid migration to form any of the other minerals, 2) primary keatite with no alteration, and 3) epitaxial orientation of the keatite with host pyroxene indicating exsolution. Nonetheless, the

This is a preprint, the final version is subject to change, of the American Mineralogist (MSA)
Cite as Authors (Year) Title. American Mineralogist, in press.
(DOI will not work until issue is live.) DOI: http://dx.doi.org/10.2138/am.2013.4170

assemblage found in Hwang, et al. (2004) may be a clue to the formation of micas found with some silica precipitates in this study.

Silica-rich mica and silica appearing as mica found in epitaxial relationship with pyroxene and amphibole (Figs. 5, 6) have been observed, in addition to keatite/amphibole precipitates. Optically, they are indistinguishable from silica precipitates that do not possess sheet silicates, and distinction is only seen at the nano-scale. We suggest later alteration and replacement of primary keatite precipitates by mica is most likely in this case. Simultaneous primary exsolution of both mica and silica is considered, but this is unlikely. Somewhat similar precipitates of thin phlogopite lamellae topotactically-exsolved in diopside in conjunction with SiO_2 polymorphs observed in Kokchetav Massif marbles (Dobrzhinetskaya, et al. 2009) may help to determine likely formation mechanism. The phlogopite + mica lamellae were interpreted as products of decompression and fluid migration in the system. Despite the fact that both phlogopite mica observed in Dobrzhinetskaya, et al. (2009) and the sheet silicates + silica observed in this study were both found in epitaxial relationship with diopside, the morphology and composition of the micas observed in this study are quite different than those of the marble study. Phlogopite lamellae were observed at the periphery of diopside grains, and adjacent to silica exsolution; micas observed in this study cover the entirety of the 'negative' pyroxene shape and are all found localized in cores of the clinopyroxene grains (Fig.2). Observation of K (Fig. 5c) in the siliceous mica (when very little to none is seen in the clinopyroxene in this study (Table 1)) is likely evidence of a replacement reaction due to fluid migration (similar to the results of Dobrzhinetskaya et al. (2009)), localized on silica during retrogression. This fluid may originate through later stage cracks and cleavages in the pyroxene. This fluid may also have

Always consult and cite the final, published document. See http://www.minsocam.org or GeoscienceWorld

originated from the clinopyroxene itself. Clinopyroxene from eclogite and granulite facies rocks can incorporate significant amounts of hydrogen. Concentrations have been shown in the range of several hundred ppm (Smyth, et al. 1991; Ingrin and Skogby 2000; Koch-Müller, et al. 2004; Katayama, et al. 2006). Other lines of evidence in favor of replacement are the degradation of the dominant interfaces of the silica-only precipitates and the anomalous silica-only EDX spectrum on the image of mica. Silica-only precipitates always display the euhedral 'negative' pyroxene form; silica + mica precipitates always display degraded pyroxene planes, likely indicating mica utilizing silica and pyroxene to form. The strange EDX spot showing only silica, but appearing as mica may be another clue to later stage reaction. Spot sizes on the TEM are extremely small and the beam may have been small enough to acquire data from the primary silica phase below the mica, without contribution from mica.

Although the associations of amphibole and mica may be important components to silica exsolution mechanisms in some rocks, they are unable to explain keatite formation. An answer may reside within the clinopyroxene itself. We propose exsolution and coalescence of vacancies contained within the UHP diopside lattice during decompression may play a large part in creating a low *P* micro-environment at the point of silica exsolution. CaEs content in pyroxenes is the result of a complex combination of rock bulk composition, *P*, and *T* (Konzett, et al. 2008; Zhao, et al. 2011), but exsolution of silica in pyroxenes has been shown to be intimately linked to the vacancy component. Substitution of CaEs component into pyroxenes results in non-stoichiometry; pyroxene may then dissolve excess silica charge balanced by vacancies in M sites (Wood and Henderson 1978). The non-stoichiometric character of HP/UHP clinopyroxene is well-established (Smyth 1980; McCormick 1986; Proyer, et al. 2004; Day and Mulcahy 2007;

Konzett, et al. 2008; Zhao, et al. 2011), and we can conclude with some confidence that vacancies were present in the UHP pyroxenes of the Kokchetav Massif garnet pyroxenite prior to decompression. The amount of vacancies is more difficult to establish, and there are other mechanisms that may form excess silica. Fortunately, clear evidence that vacancy consumption in non-stoichiometric clinopyroxene can release free silica has been produced (Day and Mulcahy 2007), although evidence for excess silica formation in both stoichiometric and non-stoichiometric pyroxenes has been found.

Calculating vacancy components in pyroxenes presents many difficulties. Vacancies have been expelled from the lattice and cannot be measured; therefore, our simple calculation of vacancies from Fe^{2+} (Table 1) is merely a potential minimum amount. This calculation will also be dependent upon trace elements that are difficult to measure by EPMA; some amounts of Cr, Sr, etc. may fill this vacancy. However, cited amounts of CaEs content in rocks can be quite high, depending upon bulk rock composition. For instance, Gasparik (1986) found CaEs values in clinopyroxenes to increase steadily and rapidly from 3.90 mol % at 1.5 GPa to 22.9 mol % at 2.8 GPa at isothermal conditions of T=1200 °C (CMAS system). In addition, oxidation of Fe^{2+} to Fe^{3+} will cause subsequent increases in the calculated vacancy component. It must be noted, however, that Na can be difficult to measure with confidence; any Na not accounted for could be enough to fill any small amount of vacancy we can possibly calculate. However, common pyroxene trace elements measured in this study (Cr, Mn) are very close to, or below detection and will not be sufficient to account for all vacancy component.

Thus, we propose an unusual mechanism for metastable keatite formation: a low pressure micro-environment created by simultaneous expulsion of silica and vacancies (in addition to hydrogen) from the destabilized UHP pyroxene lattice during slab exhumation. This mechanism is dependent upon the fact that no volume change is seen in Figs. 1 and 2, but large density changes have occurred during exsolution of silica. The precursor UHP clinopyroxene with vacancies is only slightly less dense than ~3.3 g/cm^3 — a vacancy is 0.0 g/cm^3, and keatite is the least dense silica polymorph at 2.50 g/cm^3. The local environment must accommodate density changes of ~ 1.0 g/cm^3, with no apparent volume change. The difference in densities between precursor pyroxene and current pyroxene will not account for this extreme change. Presence of metastable keatite dictates a $-\Delta P$. Thus, a low pressure micro- or nano-environment may be generated at any depth. A model portraying this possible keatite exsolution and low-pressure micro-environment formation (Fig. 7) shows a typical "precursor" euhedral clinopyroxene grain viewed approximately parallel to the *c*-axis. It contains excess silica, hydrogen, and vacancies, which are shown as a cloud in the core of the grain (Fig. 7a). Decompression causes excess material to be expelled from the pyroxene lattice. Silica and vacancies likely exsolve simultaneously, causing a large density change. Exsolution of keatite is stabilized by close lattice match to pyroxene and small precipitate size, in addition to the pressure change. Keatite exsolution is represented by black euhedral shapes in the model (Fig. 7b). Silica grows, and expulsion of small amounts of hydrogen from the host pyroxene likely causes breakdown of clinopyroxene to amphibole at clinopyroxene/keatite interfaces (Fig. 7c). Enlargement of the model clinopyroxene/keatite interface shows the position of amphibole (yellow) at interfaces, and black arrows point to a possible void (0.0 g/cm^3) created by coalesced vacancies (Fig. 7d). The polymorph of silica that exsolves is controlled by this low-pressure micro-environment, not the depth/pressure of the rock as a whole.

Here we have presented evidence confirming natural keatite in an unusual exsolution environment. Our TEM results highlight the important influence of the pyroxene/precipitate interface at the micro- and nano-scales in controlling which phases exsolve during exhumation in UHP rocks. Lines of evidence to confirm this include SAED patterns detailing the close structural relationship between host clinopyroxene and keatite, and excellent lattice matching so that dominant clinopyroxene surfaces provide templates for nano-scale keatite to nucleate. A unique exsolution mechanism takes advantage of the distinctive properties of UHP vacancy-bearing clinopyroxene, creating low-pressure micro-environments stabilized by the host pyroxene lattice. The precipitates were previously believed to be quartz, yet we show that it is unlikely that quartz nucleated and transformed to keatite in this instance. The issue of silica exsolution in HP/UHP clinopyroxene is far from resolved with this study. In fact, systematic studies of micro- and nano-scale minerals in UHP rocks is necessary to fully apprehend the influence and impact of previously-unseen minerals within the complex chemical and physical framework of exhuming rock slabs.

ACKNOWLEDGEMENTS

We thank Professor Gordon Medaris for providing his collection, and Dr. John Fournelle for assisting us during EMPA analyses. This work is supported by NSF (EAR-0810150).

References

Barnard, A. S., and Xu, H. (2008). An Environmentally Sensitive Phase Map of Titania Nanocrystals. *ACS Nano, 2*(11), 2237-2242.

Bettermann, P., and Liebau, F. (1975). The Transformation of Amorphous Silica to Crystalline Silica under Hydrothermal Conditions. *Contributions to Mineralogy and Petrology, 53*, 25-36.

Burnham, C., Clark, J., Papike, J., and Prewitt, C. (1967). A proposed crystallographic nomenclature for clinopyroxene structures. *Zeitschrift fuer Kristallographie, 125*, 109-119.

Cameron, M., and Papike, J. (1981). Structural and chemical variations in pyroxenes. *American Mineralogist, 66*, 1-50.

Carr, R. M., and Fyfe, W. S. (1958). Some observations on the crystallization of amorphous silica. *American Mineralogist, 43*, 908-916.

Cawthorn, R., and Collerson, K. D. (1974). The recalculation of pyroxene end-member parameters and the estimation of ferrous and ferric iron content from electron microprobe analyses. *American Mineralogist, 59*, 1202-1208.

Chen, J., and Fu, Z. (2006). α-PbO2-type nanophase of TiO2 from coesite-bearing eclogite in the Dabie Mountains, China-Comment. *American Mineralogist, 91*, 1699-1700.

Christie, J., Lally, J. S., Heuer, A. H., Fisher, R. M., Griggs, D. T., and Radcliffe, S. V. (1971). Comparative electron petrography of Apollo 11, Apollo 12, and terrestrial rocks. *Proceedings of the Second Lunar Science Conference. Supplement 2*, p. 69. Geochimica et Cosmochimica Acta.

Cliff, G., and Lorimer, G. W. (1975). The quantitative analysis of thin specimens. *Journal of Microscopy, 103*(2), 203-207.

Day, H., and Mulcahy, S. R. (2007). Excess silica in omphacite and the formation of free silica in eclogite. *Journal of Metamorphic Geology, 25*, 37-50.

Dobrzhinetskaya, L. F., Wirth, R., Rhede, D., Liu, Z., and Green, H. W. (2009). Phlogopite and quartz lamellae in diamond-bearing diopside from marbles of the Kokchetav massif, Kazakhstan: exsolution or replacement reaction? *Journal of Metamorphic Petrology, 27*, 607-620.

Dobrzhinetskaya, L., Schweinehage, R., Massonne, H. J., and Green, H. W. (2002). Silica precipitates in omphacite from eclogite at Alpe Arami, Switzerland: evidence of deep subduction. *Journal of Metamorphic Geology, 20*, 481-492.

Gasparik, T. (1986). Experimental study of subsolidus phase relations and mixing properties of clinopyroxene in the silica-saturated system CaO-MgO-Al2O3-SiO2. *American Mineralogist, 71*, 686-693.

Gayk, T., Kleinschrodt, R., Langosch, A., and Seidel, E. (1995). Quartz exsolution in clinopyroxene of high-pressure granulite from the Munchberg Massif. *European Journal of Mineralogy, 7*, 1217-1220.

Heaney, P. (1994). Structure and Chemistry of the Low-Pressure Slica Polymorphs. In P. J. Heaney, C. T. Prewitt, and G. V. Gibbs (Eds.), *Silica: Physical Behavior, Geochemistry and Materials Applications* (Vol. 29, pp. 1-32). Washington, D.C.: Mineralogical Society of America.

Hermann, J. (2002). Experimental constraints on phase relations in subducted continental crust. *Contributions to Mineralogy and Petrology, 143*, 219-235.

Hochella, J. M., Lower, S. K., Maurice, P. A., Penn, R. L., Sahai, N., Sparks, D. L., and Twining, B. S. (2008). Nanominerals, Mineral Nanoparticles, and Earth systems. *Science, 319*, 1631-1634.

Hochli, U., and Scott, J. F. (1971, June 28). Displacement parameter, soft-mode frequency, and fluctuations in quartz below its alpha-beta phase transition. *Physical Review letters, 26*(26), 1627-1629.

Hwang, S.-L., Shen, P., Chu, H.-T., Yui, T.-F., Liou, J. G., Sobolev, N. V., . . . Zayachkovsky, A. A. (2004). Kokchetavite: a new potassium-feldspar polymorph from the Kokchetav ultrahigh-pressure terrane. *Contributions to Mineralogy and Petrology, 148*, 380-389. doi:10.1007/s00410-004-0610-2

Ingrin, J., and Skogby, H. (2000). Hydrogen in nominally anhydrous upper-mantle minerals: concentration levels and implications. *European Journal of Mineralogy, 12*, 543-570.

Katayama, I., and Nakashima, S. (2003). Hydroxyl in clinopyroxene from the deep subducted crust: evidence for H2O transport in to the mantle. *American Mineralogist, 88*.

Katayama, I., Nakashima, S., and Yurimoto, H. (2006). Water content in natural eclogite and implication for water transport into the deep upper mantle. *Lithos, 86*, 245-259.

Katayama, I., Parkinson, C. D., Okamoto, K., Nakajima, Y., and Maruyama, S. (2000). Supercilicic clinopyroxene and silica exsolution in UHPM eclogite and pelitic gneiss from the Kokchetav massif, Kazakhstan. *American Mineralogist, 85*, 1368-1374.

Keat, P. P. (1954). A New Crystalline Silica. *Science, 120*, 328-330.

Klemd, R. (2003). Ultrahigh-pressure metamorphism in eclogites from the western Tianshan high-pressure belt (Xinjiang, western China). *American Mineralogist, 88*, 1153-1156.

Koch-Muller, M., Matsyuk, S. S., and Wirth, R. (2004). Hydroxyl in omphacites and omphacitic clinopyroxenes of upper mantle to lower crustal origin beneath the Siberian platform. *American Mineralogist, 89*, 921-931.

Konzett, J., Frost, D. J., Proyer, A., and Ulmer, P. (2008). The Ca-Eskola component in eclogitic clinopyroxene as a function of pressure, temperature, and bulk composition: an experimental study to 15 GPa with possible implications for the formation of oriented SiO2-inclusions in omphacite. *Contributions to Mineralogy and Petrology, 155*, 215-228.

Konzett, J., Libowitzky, E., Hejny, C., Miller, C., and Zanetti, A. (2008). Oriented quartz + calcic amphibole inclusions in omphacite from the Saualpe and Pohorje Mountain eclogites, Easter Alps--An assessment of possible formation mechanisms based on IR- and mineral chemical data and water storage in Easter Alpine eclogites. *Lithos*, 336-350.

Liou, J., Zhang, R. Y., Ernst, W. G., Rumble, D., and Maruyama, S. (1998). High-pressure minerals from deeply subducted metamorphic rocks. In R. Hemley (Ed.), *Ultrahigh-pressure Mineralogy: Physics and Chemistry of the Earth's Deep Interior* (Vol. 37, pp. 33-96). Mineralogical Society of America.

Martin, B. (1995). Keatite. II-Hydrothermal synthesis from silica-glass. *European Journal of Mineralogy, 7*, 1389-1397.

McCormick, T. C. (1986). Crystal-chemical aspects of nonstoichiometric pyroxenes. *American Mineralogist, 71*, 1434-1440.

Megaw, H. (1973). Crystal Structures; a Working Approach. In *Studies in Physics and Chemistry* (Vol. 10). Philadelphia: W. B. Saunders Co.

Navrotsky, A. (2004). Energetic clues to pathways to biomineralization: Precursors, clusters, and nanoparticles. *Proceedings of the National Academy of Sciences, 101*(33), 12096-12101.

O'Hara, M., and Yoder, H. S. (1967). Formation and fractionation of magmas at high pressures. *Scottish Journal of Geology, 3*, 67-117.

Okamoto, K., Liou, J. G., and Ogasawara, Y. (2000). Petrology of the diamond-grade eclogite in the Kokchetav Massif, northern Kazakhstan. *The Island Arc, 9*, 379-399.

Page, Z. F., Essene, E. J., and Mukasa, S. B. (2005). Quartz exsolution in clinopyroxene is not proof of ultrahigh pressures: Evidence from eclogites from the Eastern Blue Ridge, Southern Appalachians, U.S.A. *American Mineralogist, 90*, 1092-1099.

Proyer, A., Dachs, E., and McCammon, C. (2004). Pitfalls in geothermobarometry of eclogites: Fe3+ and changes in the mineral chemistry of omphacite at ultrahigh pressures. *Contributions to Mineralogy and Petrology, 147*, 305-318.

Proyer, A., Krenn, K., and Hoinkes, G. (2009). Oriented precipitates of quartz and amphibole in clinopyroxene of metabasites from the Greek Rhodope: a product of open system precipitation during eclogite–granulite–amphibolite transition. *Journal of Metamorphic Geology, 27*, 639-654.

Rietmeijer, F. J. (1988). Enhanced residence of submicron Si-rich volcanic particles in the stratosphere. *Journal of Volcanology and Geothermal Research, 34*, 173-184.

Shatsky, V., Sobolev, N. V., and Vavilov, M. A. (1995). Diamond bearing metamorphic rocks of the Kokchetav Massif (northern Kazakhstan). In R. Coleman, and X. Wang (Eds.), *Ultrahigh-Pressure Metamorphism* (pp. 427-455). Cambridge: Cambridge University Press.

Shau, Y.-H., Tsai, , H.-C., Liu, Y.-H., Yu, S.-C., Yang, J., and Xu, C. (2005). Transmission electron microscopic study of quartz rods with intergrown amphibole within omphacite in eclogites from the Sulu ultrahigh-pressure metamorphic terrane, eastern China. *7th International Eclogite Conference abstracts, Mitteilungen der Osterreichischen Mineralogischen Gesellschaft, 150*, 436-437.

Shropshire, J., Keat, P. P., and Vaughan, P. A. (1959). The crystal structure of keatite, a new form of silica. *Zeitschrift fur Kristallographie, 112*, 409-413.

Smith, D. (1984). Coesite in clinopyroxene in the Caledonides and its implications for geodynamics. *Nature*(310), 641-644.

Smyth, J. R. (1980). Cation vacancies and the crystal chemistry of breakdown reactions in kimberlitic omphacites. *American Mineralogist, 65*, 1185-1191.

Smyth, J., Bell, D. R., and Rossman, G. R. (1991). Incorporation of hydroxyl in upper-mantle clinopyroxenes. *Nature, 351*, 732-735.

Sobolev, N., Kuznetsova, I. K., and Zyuzin, N. I. (1968). The petrology of grospydite xenoliths from the Zagadochnaya kimberlite pipe in Yakutia. *Journal of Petrology, 9*, 253-280.

Veblen, D. R., and Cowley, J. M. (1994). Direct imaging of point defects in HRTEM. In A. Marfunin (Ed.), *Advanced Mineralogy.* Heidelberg: Springer-Verlag.

Wang, Q., Ishiwatari, A., Zhao, Z. Y., and al., e. (1993). Coesite-bearing granulite retrograded from eclogite in Weihai, eastern China. *European Journal of Mineralogy, 5*, 141-151.

Welch, M. D., and Pawley, A. R. (1991). Tremolite: New enthalpy and entropy data from a phase equilibrium study of the raction tremolite = 2 diopside + 1.5 orthoenstatite + beta-quartz + H2O. *American Mineralogist, 76*, 1931-1939.

White, J., and Corwin, J. F. (1961). Synthesis and origin of chalcedony. *The American Mineralogist, 46*, 112-119.

Williams, A. (1932). *The Genesis of the Diamond.* London: Ernest Benn Limited.

Wood, B., and Henderson, C. B. (1978). Composition and unit-cell parameters of synthetic non-stoichiometric tschermakitic clinopyroxenes. *American Mineralogist, 63*, 66-72.

Xu, H., Veblen, D. R., Luo, G., and Xue, J. (1996). Transmission electron microscopy study of the thermal decomposition of tremolite into clinopyroxene. *American Mineralogist, 81*, 1126-1132.

Zhang, L., Song, S. G., Liou, J. G., Ai, Y. L., and Li, X. P. (2005). Relict coesite exsolution in omphacite from Western Tianshan eclogites, China. *American Mineralogist, 90*, 181-186.

Zhao, S., Nee, P., Green, H. W., and Dobrzhinetskaya, L. F. (2011). Ca-Eskola component in clinopyroxene: Experimental studies at high pressures and high temperatures in multianvil apparatus. *Earth and Planetary Science Letters, 307*(3-4), 517-524.

Figure Captions

Figure 1. Transmitted light photomicrographs of Kokchetav Massif clinopyroxenes. (a) The core of a clinopyroxene looking parallel to the *c*-axis. The dark euhedral dots are siliceous precipitates. (b) Two different clinopyroxene grains, (junction shown by two arrows), both viewed at a high angle to the *c*-axis. Here the precipitates appear as rods, rather than dots, illustrating a definite crystallographic relationship between precipitates and host clinopyroxene. Precipitates are concentrated in the cores and no precipitates have formed at grain boundaries. Also note the lack of deformation surrounding the precipitates (i.e. no apparent volume change

cracks). This indicates the precipitates have likely not transformed to quartz from a denser phase such as coesite. The grains are quite fresh, with little alteration.

Figure 2. (a) TEM image of keatite precipitate (bright shape in center) growing epitaxially within host clinopyroxene (dark area surrounding keatite), and amphibole (gray mineral indenting keatite). Image shows negative pyroxene shape of keatite with dominant pyroxene crystal planes {100}, {010}, and {110} labeled. (b) Selected Area Electron Diffraction (SAED) pattern of host CPX (no arrows, zone axis [001]), keatite precipitates (white left-pointing arrows, zone axis [010]), and amphibole (right-pointing black arrows, zone axis [001]). (c, d) Schematic indexing of keatite (c), and keatite plus CPX (d). Keatite spots which appear in the SAED, (100) and (001), are typically at extinction, but appear due to multiple diffraction. These spots are X's in the simulated diffraction patterns (c, d). EDS spectrum from keatite (inset in (a)) show precipitate is a silica polymorph. Carbon peak is from coated carbon.

Figure 3. HRTEM image of an interface between host CPX and amphibole precipitate from Fig. 4, with FFT patterns from host CPX (top right) and amphibole precipitate (lower right). Along the *b*-direction, CPX lattice periodicity is half of the amphibole lattice. Arrows point to the same indexed *hkl*'s in both minerals; the (020) diffraction spot for amphibole is approximately half the distance of CPX (020) from (000).

Figure 4. Schematic representation of the structural relationship between CPX and keatite lattices based upon the SAED pattern, illustrating crystallographic relationship of keatite to host CPX. (a, c) represent the same orientations: $[001]_{\mathrm{CPX}} \parallel [100]_{\mathrm{keatite}}$. The initial layer (Fig. 4a) of

keatite tetrahedra (green) bonding to clinopyroxene tetrahedra (blue) closely matches clinopyroxene lattice dimensions with systematic gaps of keatite tetrahedra in the structure. (c) subsequent layers of keatite tetrahedra have been added to the structure. (b) Systematic tetrahedra absences are seen in the *a*-*b* clinopyroxene section. Red arrows in all orientations denote the location of the first layer of bonding for reference. (d) comparison of the clinopyroxene/keatite unit cells in the same orientation as a and c, along clinopyroxene *b*-axis and keatite *c*-axis demonstrates that the clinopyroxene lattice is a mere 3.5% larger than keatite over just one unit cell. Even less difference is seen along keatite *b*-axis/clinopyroxene *c*-axis.

Figure 5. STEM image of a precipitate exhibiting alteration to super-siliceous mica. (a) a typical 'negative' pyroxene-shaped silica has been largely altered to mica. Although the image (a) and image of spot 1 inset into the EDS spectrum show mica layering, the EDS spectrum collected at spot 1 shows only silica (b). (c) EDS spectrum from the center of the altered precipitate at spot 2 indicates this area is high silica mica. In these altered precipitates, the negative pyroxene shape with dominant crystal faces is nearly unrecognizable-dominant CPX (010), (110) interfaces are quickly destroyed as the silica is replaced by sheet silicate. A white arrow on the left side of the image (a) points to a degraded (110) face. HRTEM lattice images of spots 3 and 4, amphibole and mica, respectively, are clarified in Fig. 6.

Figure 6. HRTEM lattice images of amphibole/CPX (e) and mica/CPX (f) interfaces from Fig. 8 (labeled areas 3 and 4, respectively). (a) SAED pattern shows all three phases found in this precipitate — CPX, amphibole, mica. All three phases have parallel (010) planes and $[100]_{\mathrm{CPX}}$

$\parallel[001]_{\text{mica}}$. This can also be seen in simulations of mica SAED patterns (d) and CPX, amphibole, mica SAED patterns (b). A degraded (110) pyroxene plane can be seen in (f).

Figure 7. Possible keatite precipitate formation model. (a) A typical *c*-axis CPX grain filled with excess silica, H^+, and vacancies (Ca-Eskola component). As the rock slab begins decompression, the pyroxene structure destabilizes and excess material is pushed out of the lattice. (b) Silica nucleates and grows in the core of the CPX, taking on the CPX shape. (c) CPX transforms to amphibole, and vacancies exsolve and coalesce. (d) Detail of silica precipitate shows position of amphibole and black arrows point to a void of coalesced vacancies. A low pressure micro-environment may be formed from density changes between silica and pyroxene, aided by coalescing vacancies of no density.

This is a preprint, the final version is subject to change, of the American Mineralogist (MSA)
Cite as Authors (Year) Title. American Mineralogist, in press.
(DOI will not work until issue is live.) DOI: http://dx.doi.org/10.2138/am.2013.4170

.

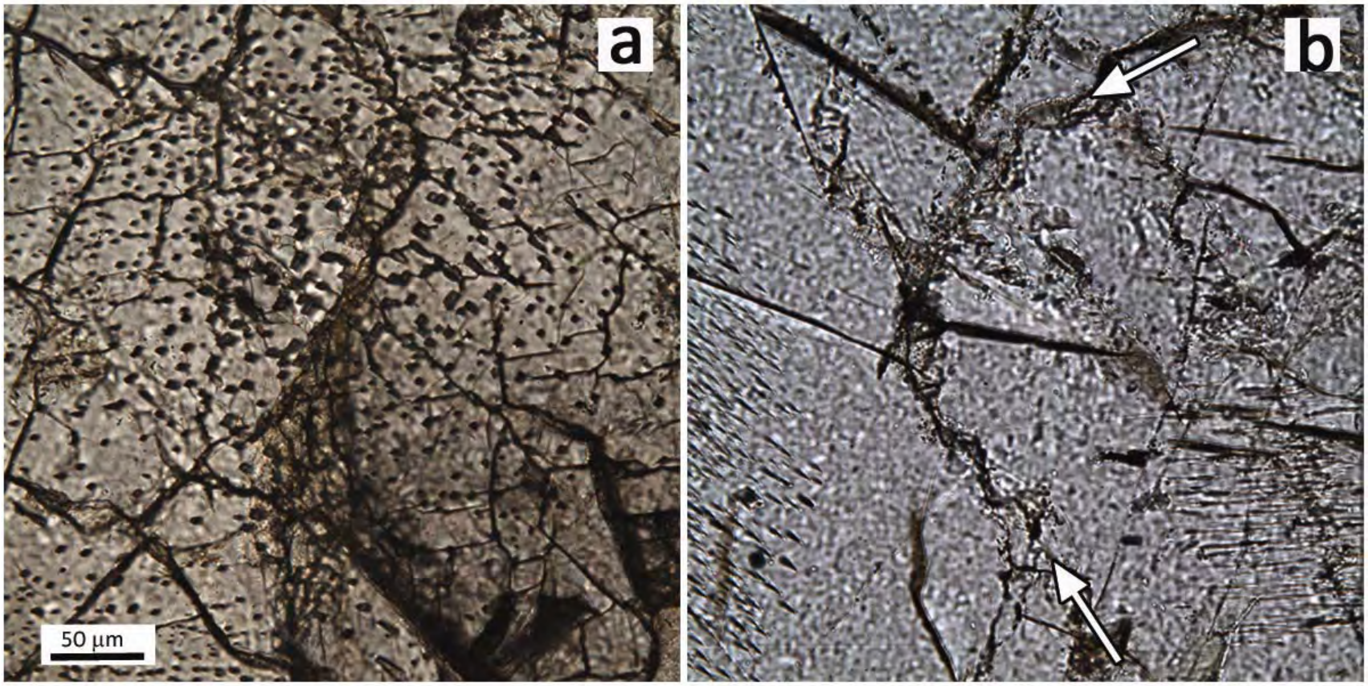

Figure 1. Transmitted light photomicrographs of Kokchetav Massif clinopyroxenes. (a) The core of a clinopyroxene oriented nearly parallel to the *c*-axis. The dark euhedral dots are siliceous precipitates. (b) Two different clinopyroxene grains, (junction shown by two arrows), both viewed at a high angle to the *c*-axis. Here the precipitates appear as rods, rather than dots, illustrating a definite crystallographic relationship between precipitates and host clinopyroxene. Precipitates are concentrated in the cores and no precipitates have formed at grain boundaries. Also note the lack of deformation surrounding the precipitates (i.e. no apparent volume change cracks). This indicates the precipitates have likely not transformed to quartz from a denser phase such as coesite. The grains are quite fresh, with little alteration.

Always consult and cite the final, published document. See http://www.minsocam.org or GeoscienceWorld

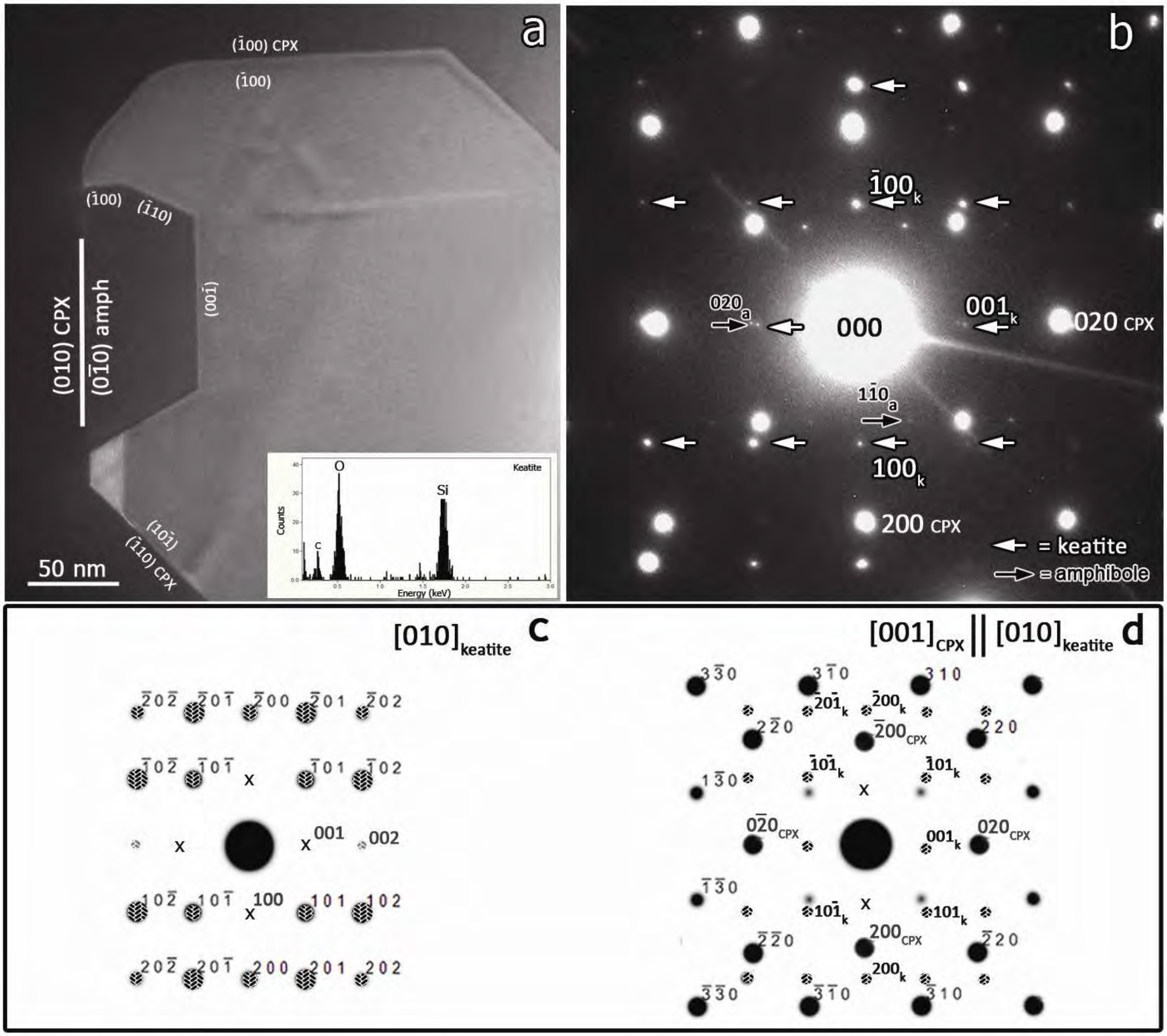

Figure 2 (a) TEM image of keatite precipitate (bright shape in center) growing epitaxially within host clinopyroxene (dark area surrounding keatite), and amphibole (gray mineral indenting keatite). Image shows negative pyroxene shape of keatite with dominant pyroxene crystal planes {100}, {010}, and {110} labeled. (b) Selected Area Electron Diffraction (SAED) pattern of host CPX (no arrows, zone axis [001]), keatite precipitates (white left-pointing arrows, zone axis [010]), and amphibole (right-pointing black arrows, zone axis [001]). (c,d) Schematic indexing of keatite (c), and keatite plus CPX (d). Keatite spots which appear in the SAED, (100) and (001), are typically at extinction, but appear due to multiple diffraction. These spots are X's in the simulated diffraction patterns (c,d). EDS spectrum from keatite (inset in (a)) show precipitate is a silica polymorph. Carbon peak is from coated carbon.

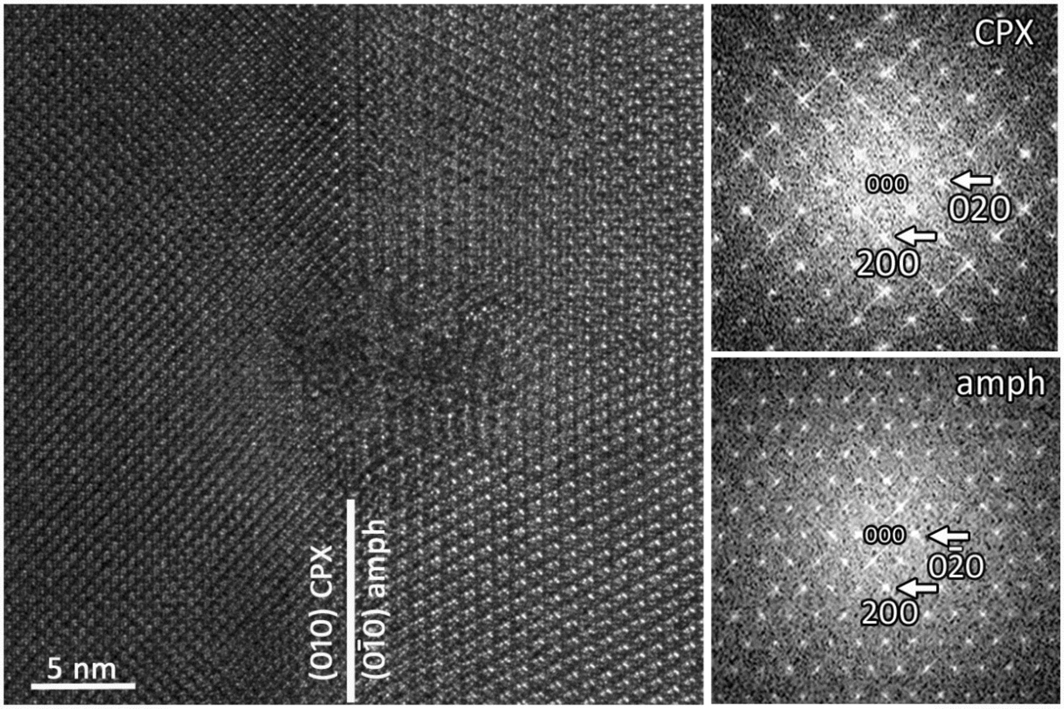

Figure 3 HRTEM image of an interface between host CPX and amphibole precipitate from Fig. 4, with FFT patterns from host CPX (top right) and amphibole precipitate (lower right). Along the *b*-direction, CPX lattice periodicity is half of the amphibole lattice. Arrows point to the same indexed *hkl*'s in both minerals; the (020) diffraction spot for amphibole is approximately half the distance of CPX (020) from (000).

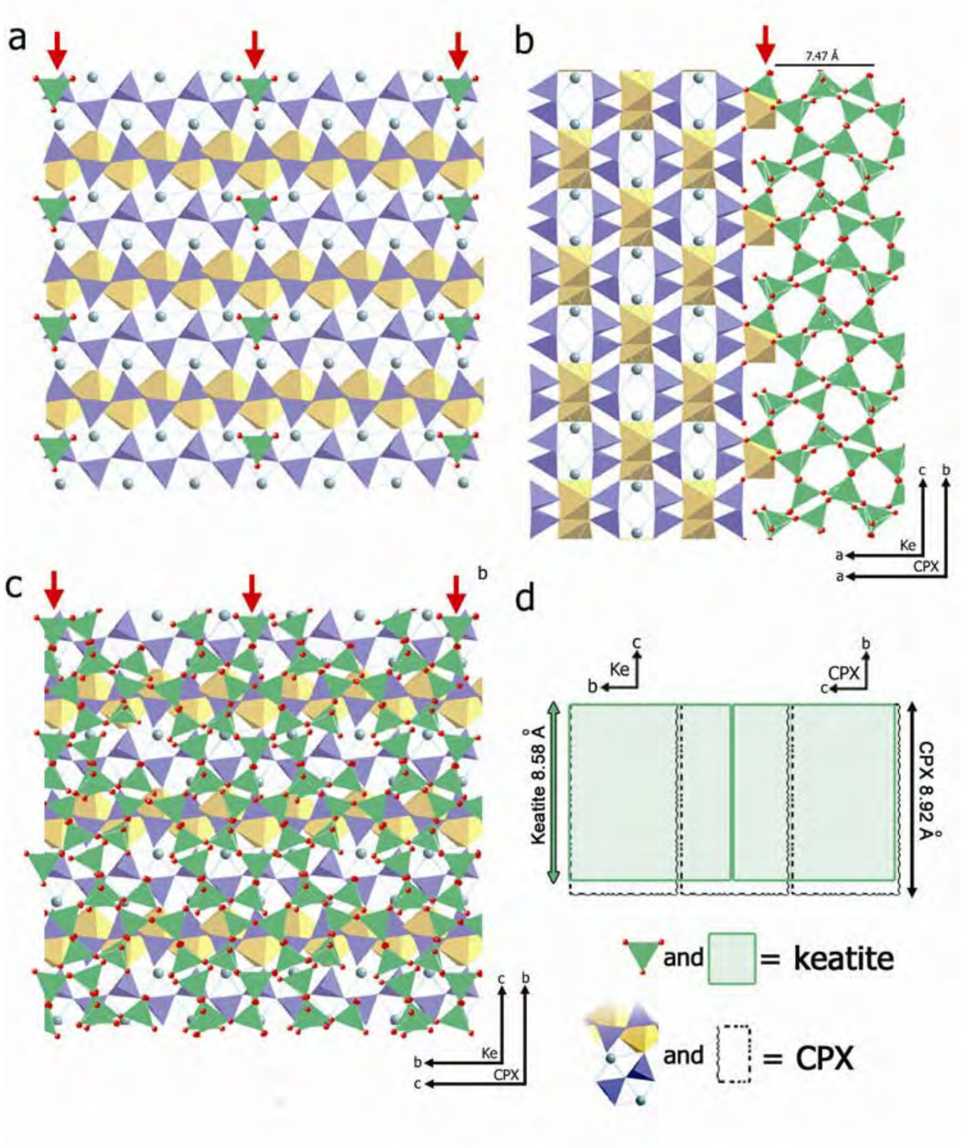

Figure 4 Schematic representation of the structural relationship between CPX and keatite lattices based upon the SAED pattern, illustrating crystallographic relationship of keatite to host CPX. (a)The initial layer of green keatite tetrahedra bonding to blue tetrahedra in CPX matches CPX lattice dimensions nicely with little to no rotation of the tetrahedra. For this to work, systematic gaps of keatite tetrahedra are created. These can also be seen in (b) where the orientation is keatite [010]‖CPX [001]. Red arrows in each model denote location of the first layer of bonding. (d) Illustrates lattice match over three unit cells of CPX and two keatite unit cells along CPX *b*-axis and keatite *c*-axis; CPX lattice is a mere 3.5% larger than keatite. In (c), subsequent layers of tetrahedra have been added to the layered structure in the same orientation as (a).

This is a preprint, the final version is subject to change, of the American Mineralogist (MSA)
Cite as Authors (Year) Title. American Mineralogist, in press.
(DOI will not work until issue is live.) DOI: http://dx.doi.org/10.2138/am.2013.4170

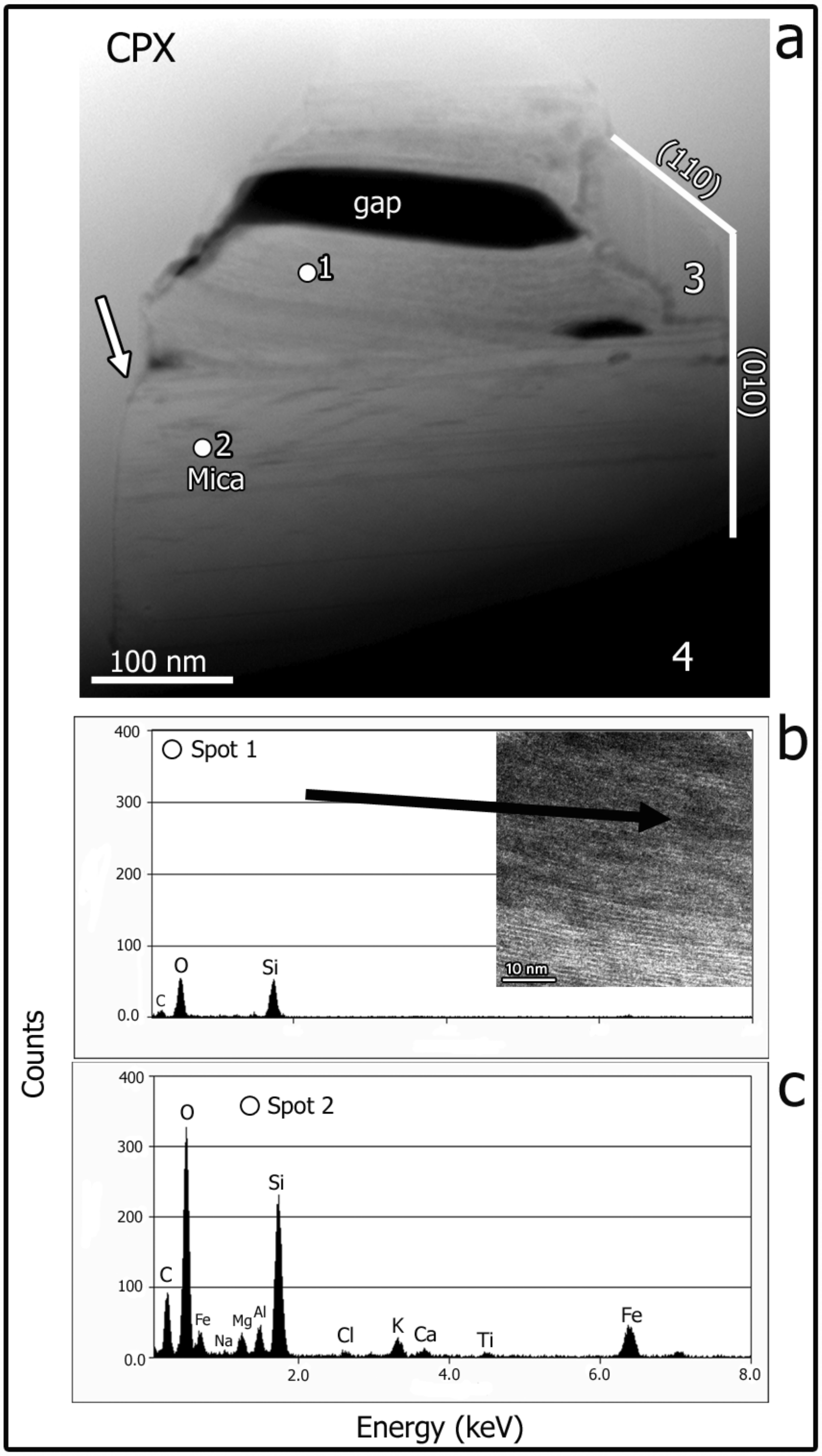

Figure 5 STEM image of a precipitate exhibiting alteration to super-siliceous mica. (a) a typical 'negative' pyroxene-shaped silica has been largely altered to mica. Although the image (a) and image of spot one inset into the EDS spectrum shows mica layering, the EDS spectrum collected at spot 1 shows only silica (b). (c) EDS spectrum from the center of the altered precipitate at spot 2 indicates this area is high silica mica. In these altered precipitates, the negative pyroxene shape with dominant crystal faces is nearly unrecognizable-dominant (010), (110) interfaces are quickly destroyed as the silica is replaced by sheet silicate. A white arrow on the left side of the image (a) points to a degraded (110) face. HRTEM lattice images of spots 3 and 4, amphibole and mica, respectively, is clarified in Fig. 6.

Always consult and cite the final, published document. See http://www.minsocam.org or GeoscienceWorld

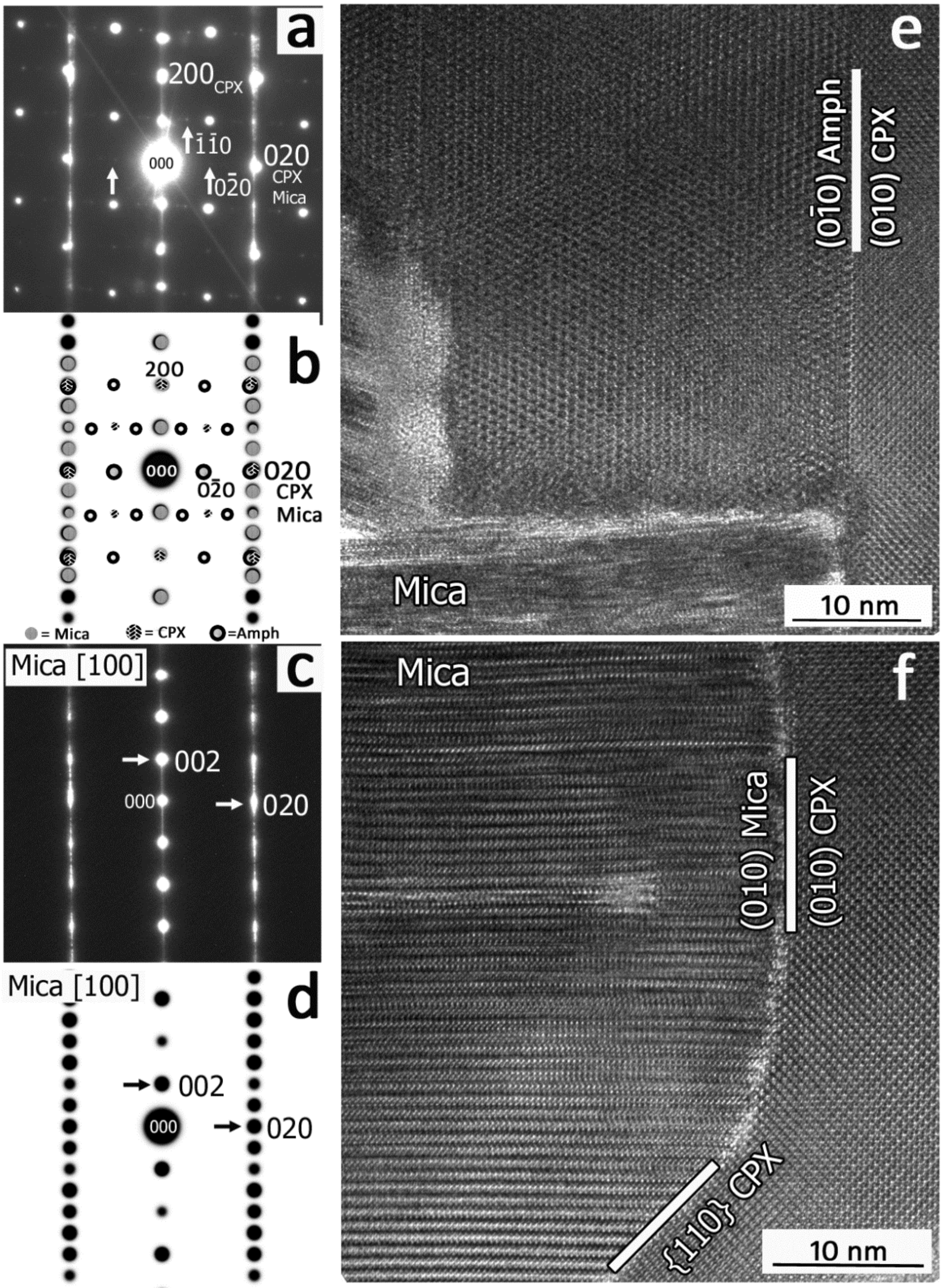

Figure 6. HRTEM lattice images of amphibole/CPX (e) and mica/CPX (f) interfaces from Fig. 8 (labeled areas 3 and 4, respectively). (a) SAED pattern shows all three phases found in this precipitate—CPX, amphibole, mica. All three phases have parallel (010) planes and $[100]_{CPX} \parallel [001]_{mica}$. This can also be seen in simulations of mica SAED patterns (d) and CPX, amphibole, mica SAED patterns (b). A degraded (110) pyroxene plane can be seen in (f).

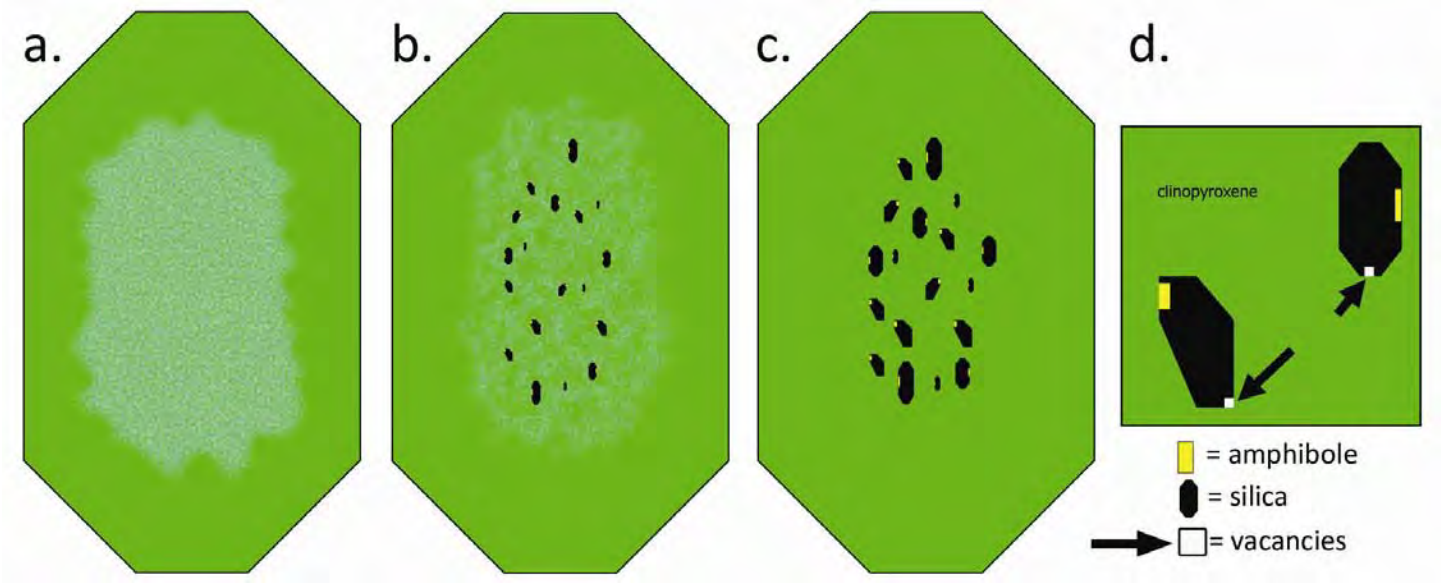

Figure 7 Keatite precipitate formation model. (a) A typical *c*-axis CPX grain filled with excess silica, H^+, and vacancies (Ca-Eskola component). As the rock slab begins decompression, the pyroxene structure destabilizes and excess material is pushed out of the lattice. (b) Silica nucleates and grows in the core of the CPX, taking on the CPX shape. (c) Some form of water allows CPX to transform to amphibole, and vacancies exsolve and coalesce. (d) Close-up of silica precipitate shows position of amphibole and black arrows point to a void of coalesced vacancies. The silica polymorph that nucleates is likely dictated by the core structure of the pyroxene, and the low-pressure micro-environment created by negative density changes and a possible vacuum formed by the exsolution of vacancies.

Wt. % Oxide	**Pt. 1**	**Pt. 2**	**Pt. 3**	**Pt. 4**	**Pt. 5**	**Pt. 6**	**Pt. 7**	**Pt. 8**	**Pt. 9**	**Pt. 10**	**Pt. 11**	**Pt. 12**	**Pt. 13**	**Pt. 14**	**AVG**	**STDEV**	**SERR**
SiO_2	53.68	53.54	54.16	53.22	54.24	53.72	53.87	53.54	53.56	54.03	53.59	53.69	54.19	53.76	53.77	0.28	0.08
TiO_2	0.21	0.11	0.12	0.07	0.08	0.08	0.09	bd	0.11	0.03	bd	0.07	0.10	0.13	0.10	0.04	0.02
Al_2O_3	2.48	2.37	2.35	2.58	2.28	2.38	2.30	2.38	2.39	2.47	2.38	2.30	2.24	2.29	2.37	0.09	0.02
Cr_2O_3	bd	bd	bd	bd	bd	bd	bd	bd	bd	bd	bd	bd	bd	bd	bd	bd	0.02
FeO	6.30	6.39	6.36	6.77	6.62	6.53	6.75	6.64	6.70	6.61	6.65	6.37	6.57	6.14	6.53	0.18	0.05
MnO	0.06	0.08	0.05	0.14	0.09	0.13	0.08	0.12	0.10	0.14	0.15	0.04	0.18	0.02	0.10	0.04	0.01
MgO	13.26	13.37	13.17	13.55	13.12	13.09	13.46	13.27	13.32	13.21	13.12	13.34	13.31	13.22	13.27	0.13	0.04
CaO	23.19	22.98	22.89	22.66	22.79	22.59	22.89	22.97	22.75	22.82	22.90	23.08	22.58	22.84	22.85	0.17	0.05
Na_2O	0.70	0.82	0.73	0.81	0.88	0.79	0.84	0.87	0.79	0.77	0.81	0.81	0.82	0.81	0.80	0.05	0.01
K_2O	0.07	0.05	0.04	0.02	0.05	0.11	0.03	0.03	0.04	0.17	0.03	0.04	0.02	0.03	0.05	0.04	0.01
Total	99.94	99.70	99.88	99.82	100.15	99.40	100.31	99.81	99.76	100.26	99.63	99.74	100.01	99.25			
Si	1.978	1.981	1.994	1.968	1.997	1.991	1.981	1.981	1.982	1.987	1.985	1.984	1.993	1.992	*Notes for Table 1:*		
Ti	0.006	0.003	0.004	0.002	0.002	0.002	0.003	bd	0.003	0.001	bd	0.002	0.003	0.004		bd = below detection	
^{IV}Al	0.022	0.019	0.006	0.032	0.003	0.009	0.019	0.019	0.018	0.013	0.015	0.016	0.007	0.008		[]=vacancy component (CaEs)	
^{VI}Al	0.086	0.084	0.096	0.080	0.096	0.095	0.081	0.085	0.086	0.094	0.089	0.085	0.090	0.092		Cations per 6 O	
Cr	bd	bd	bd	bd	bd	bd	bd	bd	bd	bd	bd	bd	bd	bd		Oxygen calculated	
Fe^{2+}	0.194	0.198	0.196	0.209	0.204	0.202	0.208	0.205	0.207	0.203	0.206	0.197	0.202	0.190	*Statistics:*		
Mn	0.002	0.003	0.002	0.004	0.003	0.004	0.002	0.004	0.003	0.004	0.005	0.001	0.005	0.001		n=14	
Mg	0.729	0.737	0.723	0.747	0.720	0.723	0.738	0.732	0.734	0.724	0.724	0.735	0.730	0.730		AVG= average	
Ca	0.916	0.911	0.903	0.898	0.899	0.897	0.902	0.911	0.902	0.899	0.909	0.914	0.890	0.907		STDV= standard deviation	
Na	0.050	0.059	0.052	0.058	0.063	0.056	0.060	0.062	0.057	0.055	0.058	0.058	0.059	0.058		SERR= standard error	
K	0.003	0.002	0.002	0.001	0.002	0.005	0.002	0.001	0.002	0.008	0.002	0.002	0.001	0.001			
[]	0.014	0.003	0.022	0.001	0.011	0.015	0.005	0.000	0.005	0.011	0.007	0.006	0.019	0.017			
Cations per 6 O	4.000	4.000	4.000	4.000	4.000	4.000	4.000	4.001	4.000	4.000	4.000	4.000	4.000	4.000			

Table 1. Recalculated EMPA clinopyroxene analyses from Kokchetav Massif CPX grain, calculated with all iron as Fe2+. Measurements made with 1µm beam. Oxygen calculated, all calculations based on 6 O. Minimum potential calculated vacancy component = ([]).